Supplementary Information for Strongly coupled exciton - surface lattice resonances engineer long-range energy propagation

Ravindra Kumar Yadav,[1] Matthew Otten,[2] Weijia Wang,[3] Cristian L. Cortes,[2] David J. Gosztola,[2] Gary P. Wiederrecht,[2] Stephen K. Gray,[2] Teri W. Odom,[3,4,5] and Jaydeep Kumar Basu[1]

[1]*Department of Physics, Indian Institute of Science, Bangalore, India.*

[2]*Center for Nanoscale Materials, Argonne National Laboratory, Lemont, IL 60439, USA.*

[3]*Graduate Program in Applied Physics, Northwestern University, Evanston, Illinois 60208, USA.*

[4]*Department of Materials Science and Engineering, Northwestern University, Evanston, Illinois 60208, USA.*

[5]*Department of Chemistry, Northwestern University, Evanston, Illinois 60208, USA.*

(Dated: May 29, 2020)

Abstract

Here, we provide the details of sample preparation, experimental set up, characterization of samples, and additional computational results.

CONTENTS

SEMICONDUCTOR QUANTUM DOT PHOTOLUMINESCENCE (PL) AND ABSORPTION SPECTRA

To measure the semiconductor quantum dot (SQD) PL and absorption spectra, a SQD solution was prepared by dissolving cleaned SQDs in toluene. Figure S1 shows an absorption spectrum for a SQD solution, measured with a Perkin-Elmer UV-Vis spectrometer and the corresponding photoluminescence (PL) spectra, measured with a Perkin-Elmer fluorescence spectrometer.

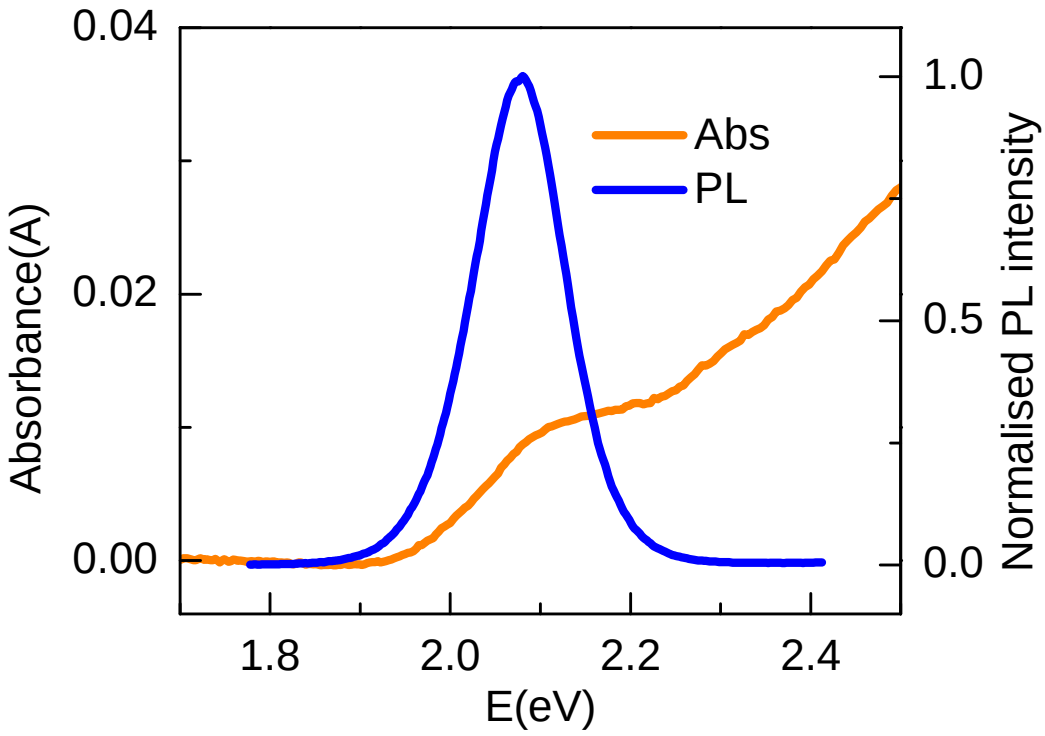

FIG. S1: PL and absorption spectra of a SQD solution.

SQD/PLASMON LATTICE SAMPLE PREPARATION

We prepared two types of SQD/plasmon lattice system, which we term as *C*-configuration and *R*-configuration. The former corresponds to a close-packed configuration and the latter to a randomly distributed configuration of SQDs. For the *C*-configuration discussed in the main text, stacks of 100 nm thick compact layers of SQDs were deposited on a plasmon lattice using the Langmuir-Schaefer (LS) deposition technique [1–3]. In the LS deposition technique, a hydrophobic SQD solution in chloroform is spread drop by drop on a water surface of a Langmuir-Blodgett (LB) trough until the pressure reaches saturation level. Finally, the SQD monolayer on the water surface is compressed through barriers until the pressure reaches ≈ 40 mN/m which is the optimal pressure for compact SQD monolayer formation as shown in Fig. S2. The SQD monolayer is transferred onto the plasmon lattice at the same pressure. To deposit 100 nm thick stack of SQD layers, ten monolayers of SQDs are transferred onto the plasmon lattice at the same pressure (≈ 40 mN/m) indicated by the red arrow in Fig. S2. The *R*-configuration is prepared by simply spin coating a SQD solution in toluene (1mM) onto the plasmon lattice with speed 3000rpm and time

60 seconds.

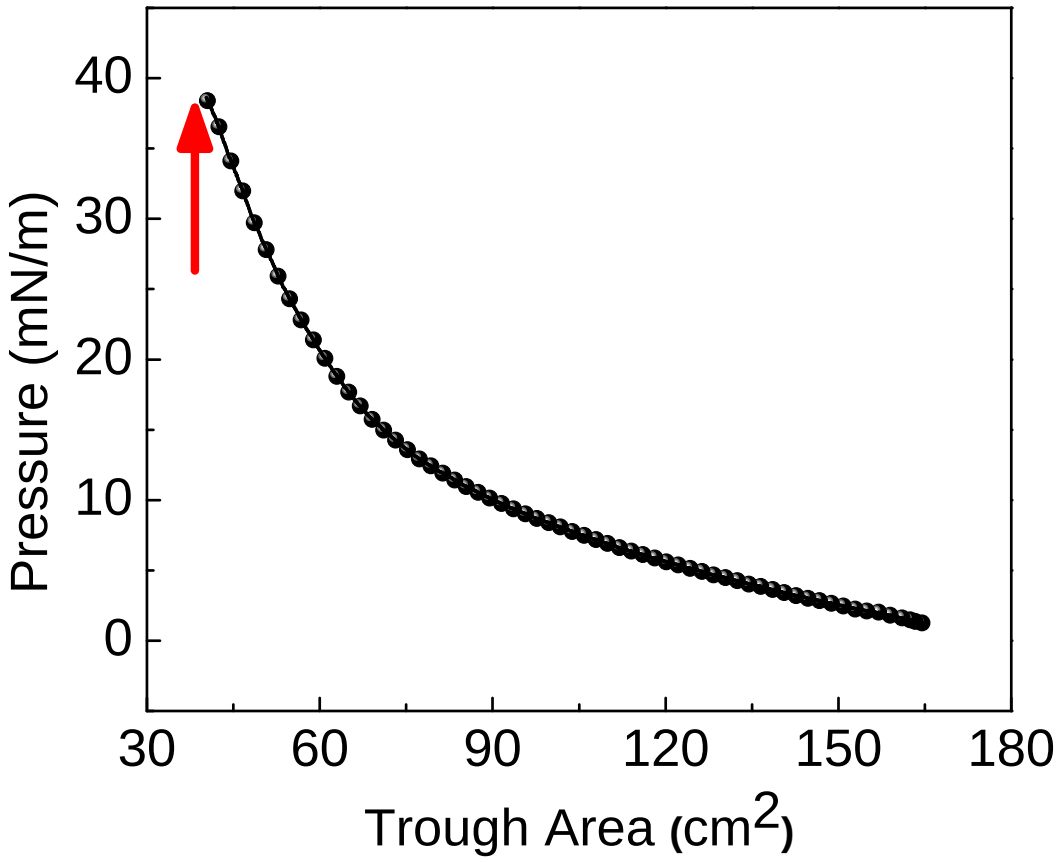

FIG. S2: Pressure vs trough area. SQD monolayers were transferred onto a plasmon lattice at pressure 38mN/m and trough area (40cm^2) as indicated by the red arrow.

ATOMIC FORCE MICROSCOPY IMAGES OF THE SQDS/PLASMON LATTICE

Atomic force microscopy (AFM) imaging of the samples was performed using an AFM Park NX10 model in non-contact mode. Figure S3 shows AFM images after one and three SQD layer deposition onto the lattice. Generally, the films transferred by the LS technique have breakages [1, 2].

We focus on imaging these breakages in the AFM images to get the thickness of the layers as shown in the height profiles of the respective AFM images. These breakages can occur because of the larger height (40 nm) of the Ag nanoparticles (NPs) as compared to thickness of the SQD

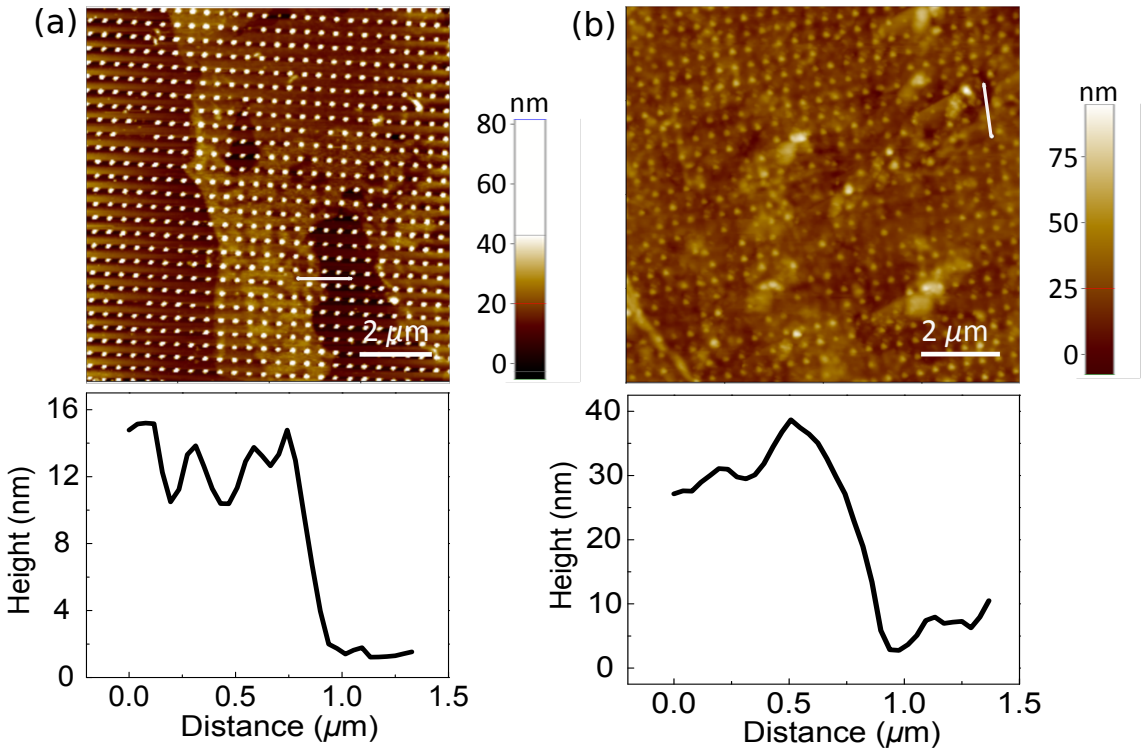

FIG. S3: (a) AFM image of plasmon lattice after transferring one SQD monolayer (top panel) with height profile near a breakage in the monolayer (bottom), showing the monolayer thickness is ≈ 10 nm. (b) AFM image of plasmon lattice after transferring three SQD monolayers (top) with height profile (bottom) near a breakage in the monolayers, showing a thickness ≈ 30 nm . Scale bar is 2 μm

layers. There are significant decreases in breakages as the thickness of SQD layer exceeds the height of Ag NPs and the SQD films look more compact.

SEMICONDUCTOR QUANTUM DOT NUMBER DENSITY (ρ)

We spread a 196ml volume (V) of SQDs with concentration (C) 10.55mg/ml on a 45 cm^2 area of a LB trough to get a single compact SQD monolayer. This allows us to calculate the expected areal number density of SQDs, n_A, in the transferred SQD monolayer on the lattice [2]:

$$n_A = \frac{3CVw}{4\pi r^3 \rho_{CdSe} A}, \tag{1}$$

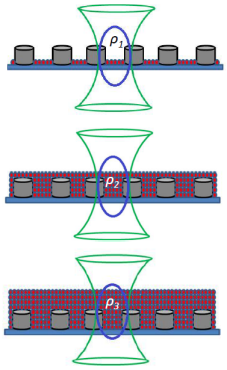

FIG. S4: Schematic for variation number of SQDs in a fixed confocal volume.

where w is the weight fraction of the olaic-acid-capped CdSe ZnS SQDs (28%) [4]. N_L is number of SQD layers, ρ_{CdSe} is the bulk density of CdSe, and r is the radius of the SQDs (4 nm). The effective SQD density ρ refers to number of SQD per unit excitation volume (V_{exc}):

$$\rho = \frac{n_A A_{exc} N_L}{V_{exc}}, \tag{2}$$

$$V_{exc} = A_{exc} t, \tag{3}$$

where $N_L = 1, 5, 10$ is the number of monolayers which leads to the three SQD number densities ρ_1, ρ_2, ρ_3, respectively. A_{exc} is the area of the laser excitation spot (laser excitation spot size for 10X objective (NA=0.20) $\sim$ 10 μm, and t is depth of excitation field ($\sim$ 10 μm,). This density is changed by changing the thickness of the SQD layers which is shown schematically in Fig. S4.

COMPARISON OF PL SPLITTING IN THE C_3 AND R CONFIGURATIONS

We compare PL splitting in the C_3 and R configurations of the SQDs on the plasmon lattice. The thickness of the SQD layer for the R and C_3 configurations were kept approximately similar but the SQDs were arranged randomly in the R configuration whereas in C_3, they were more ordered. Figure S5 gives the corresponding PL spectra, showing smaller splitting, and thus coupling, for the R-configuration relative to the C-configuration.

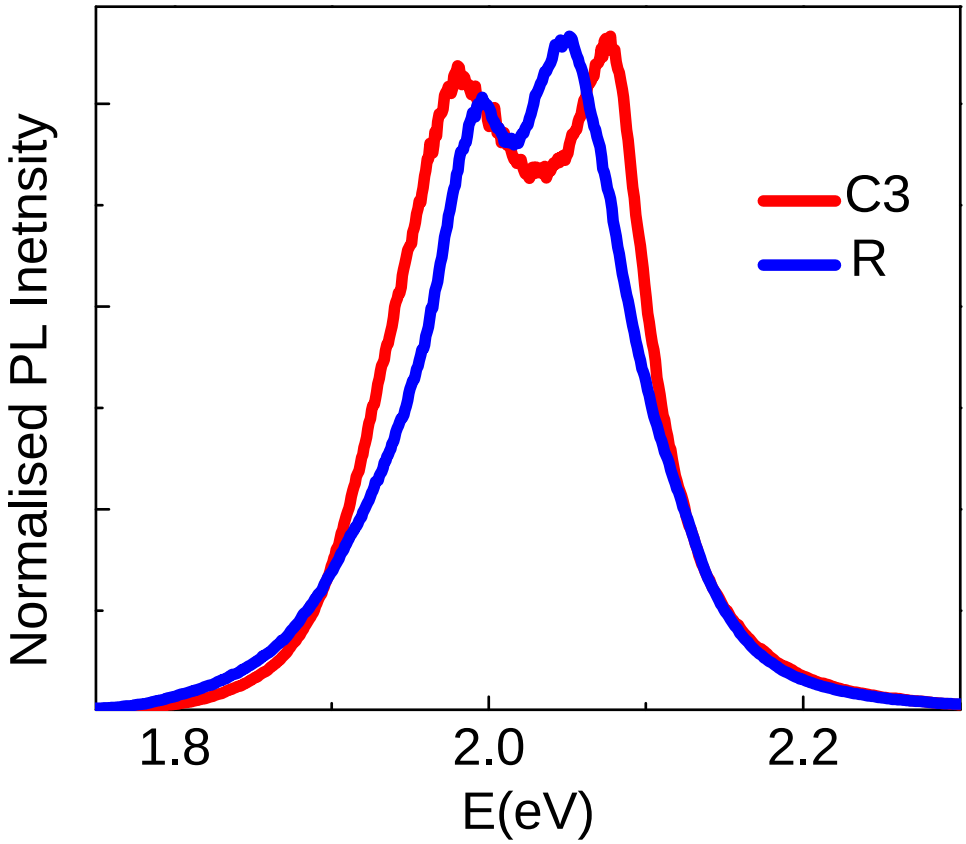

FIG. S5: Comparison of coupling strength between C and R configurations.

SEMICONDUCTOR QUANTUM DOT DENSITY DEPENDENT TRANSMISSION AND PL SPECTRA

We confirm experimentally, that a red-shift in the plasmon lattice resonance does occur in the presence of the semiconductor quantum dots. We present the results in Fig. S6(a) below, showing such red-shifts, for the C_2 and C_3 configurations. Compared to the bare plasmon lattice case (with a peak at 2.1 eV), the C_2 and C_3 configurations show an extinction peak that is shifted by 60 and 85 meV respectively. However, splitting could be just combination of red shift of SLR and blue shift of SQD but we should emphasize that this shift is not consistent with the photoluminescence peaks from light emitted by the quantum dots (Fig. S6(a) of the main manuscript, and Fig. S6(b) below). The photoluminescence peaks are closer to 2.1 eV and do not match the extinction peaks from Fig. S6(a). This suggests that the red-shift is an independent effect that is not attributed to the

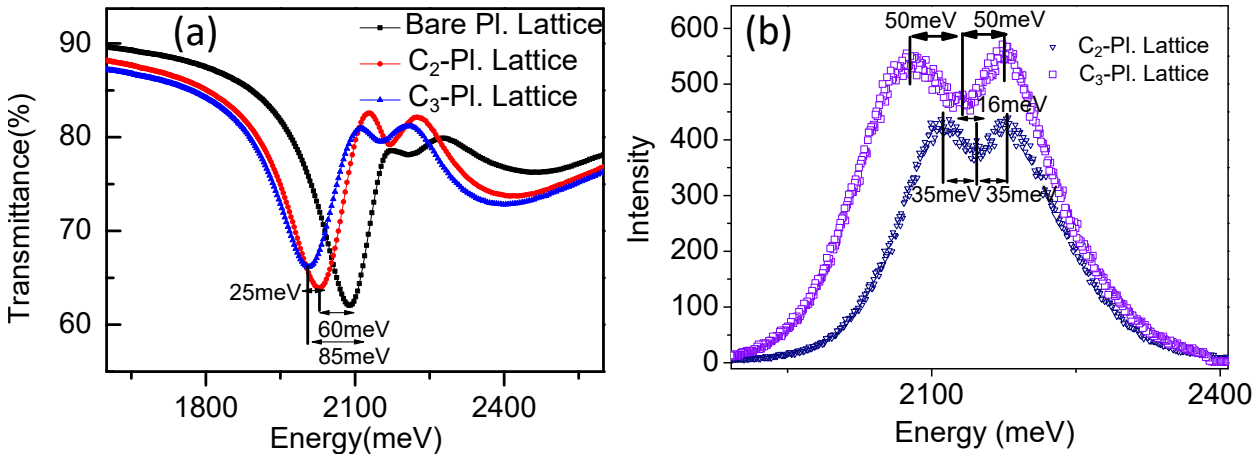

FIG. S6: (a) Transmission spectra of plasmon lattice prior to SQD coating (denoted as Bare Pl. Lattice) and after coating with C_2 and C_3 SQD configurations (denoted as C_2-Pl. Lattice and C_3-Pl. Lattice). The black arrows show the shifts in the main transmission dip due to the SQD layers. (b) Photoluminescence spectra for the C_2 and C_3 configurations of SQDs on the plasmon lattice. The black arrows show the peak shifts of relative to the dip.

strong coupling, coherent interaction and does not affect the main results from the manuscript.A blue shift of QD emission when interacting with plasmons, particularly due to enhanced rates of QD excitation that begin to show blue shifted biexciton emission[5]. However, this process is optical excitation intensity dependent, with higher optical intensities producing more biexcitons and a stronger blue shift. We effectively have an intensity dependent study due to the 3 concentrations of SQDs used, with high concentrations resulting in fewer photoexcitations per SQD, at fixed incident excitation intensity. Interestingly, no such blue shift is observed (see Figure 3(b) in manuscript).

EXPERIMENTAL SETUP FOR DISTANCE-DEPENDENT PL SPECTRA

All steady-state distance-dependent PL spectra were collected using a Model ”WITec alpha SNOM” instrument in transmission mode as shown in Fig. S7. The plasmon lattice was overlaid with SQDs and excited by a 10X (NA=0.20) objective from the top and distance-dependent PL spectra were collected from the bottom objective.

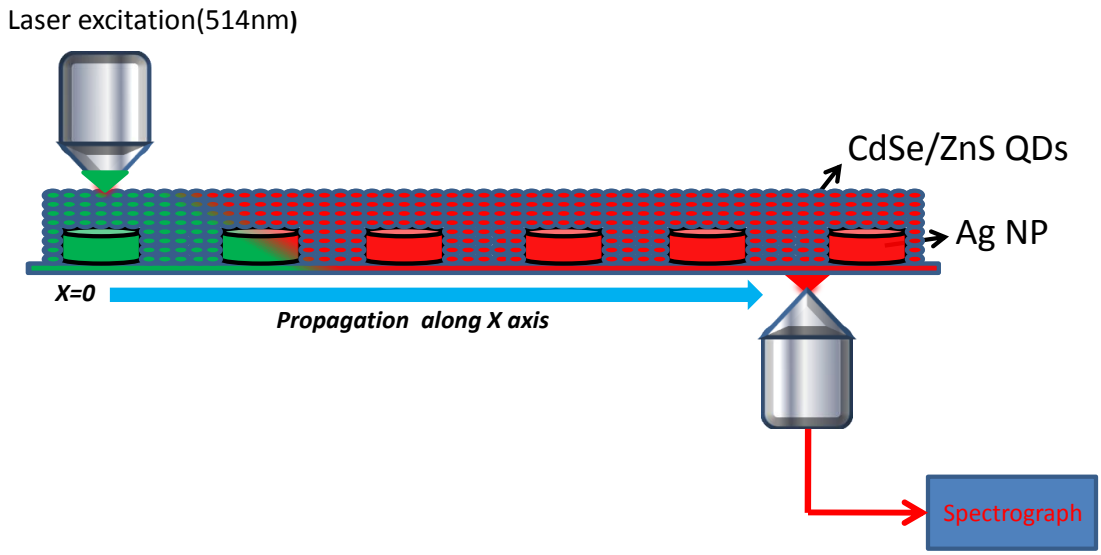

FIG. S7: Schematic for measurement of the distance dependence of the steady state PL rate.

PHOTOLUMINESCENCE (PL) MAP OF THE SQDS/PLASMON LATTICE

A PL map was collected by exciting the SQDs/Plasmon system with a unpolarised 514 nm laser and PL emission was collected using a 10X objective. Here, both the excitation and collection objectives were aligned while collecting the PL maps. Figure S8 shows the resulting maps for $X = 0$ and 2000 μm. Each map is scanned over $\approx 70 - 80$ μm. The PL intensity appears more or less homogeneous in these regions. Our PL distance-dependent intensity profiles (fixed excitation and variable collection) are obtained along such homogeneous regions.

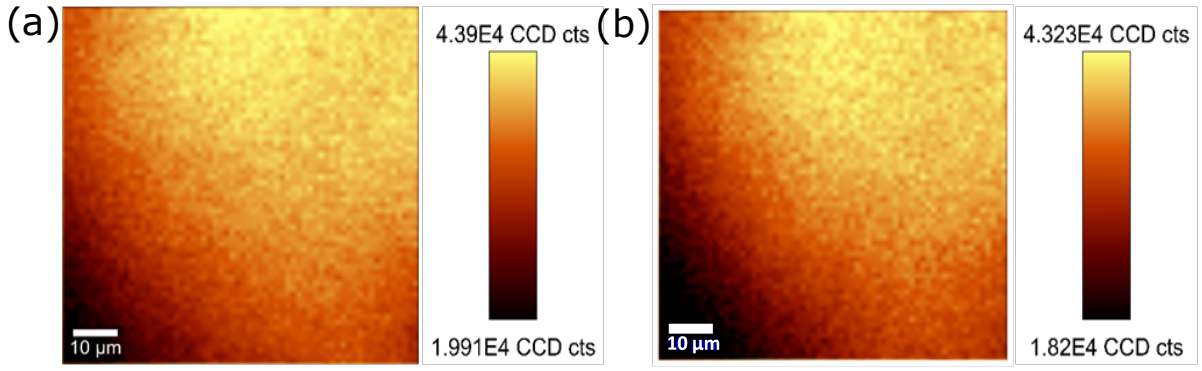

FIG. S8: (a) PL map of an excited SQD region at X = 0 μm. (b) PL map of a SQD region a distance X = 2000 μm.

$X(\mu\text{m})$	0	60	120	180	280	500	600
$2g(X)$(meV)	93	97	97	71	62	57	50

TABLE I: Values of splitting (meV) at various positions, $X(\mu\text{m})$.

DISTANCE DEPENDENCE OF THE PL SPECTRAL SPLITTING OF THE SQD/PLASMON LATTICE

The distance or X dependence of the PL spectra of the SQD/plasmon lattice systems was measured by exciting the sample with a top objective, 10X (NA=0.20) using unpolarised 514 nm CW laser and collecting the PL from a movable bottom objective 10X (NA=0.30) in transmission mode. To measure the PL from SQD regions displaced from the excitation region, the bottom objective was moved in the X-direction as shown in Fig. 4 of the main text with additional PL spectra in Fig. S9. These results show the PL splitting spectra of the SQDs/Plasmon lattice at different X positions for both forward and reverse scanning of the bottom objective. The similar variation in the PL spectra for forward and reverse movement of the bottom objective allows us to rule out the effect of local SQD structural variation on the distance dependence of the PL spectra. Table I shows the values of splitting (or $2g$, where g is the coupling strength) for various X values. Note that these splittings are inferred by fitting two Lorentzian functions to the experimental spectra and defining the splitting as the difference between the centres of the two underlying Lorentzians.

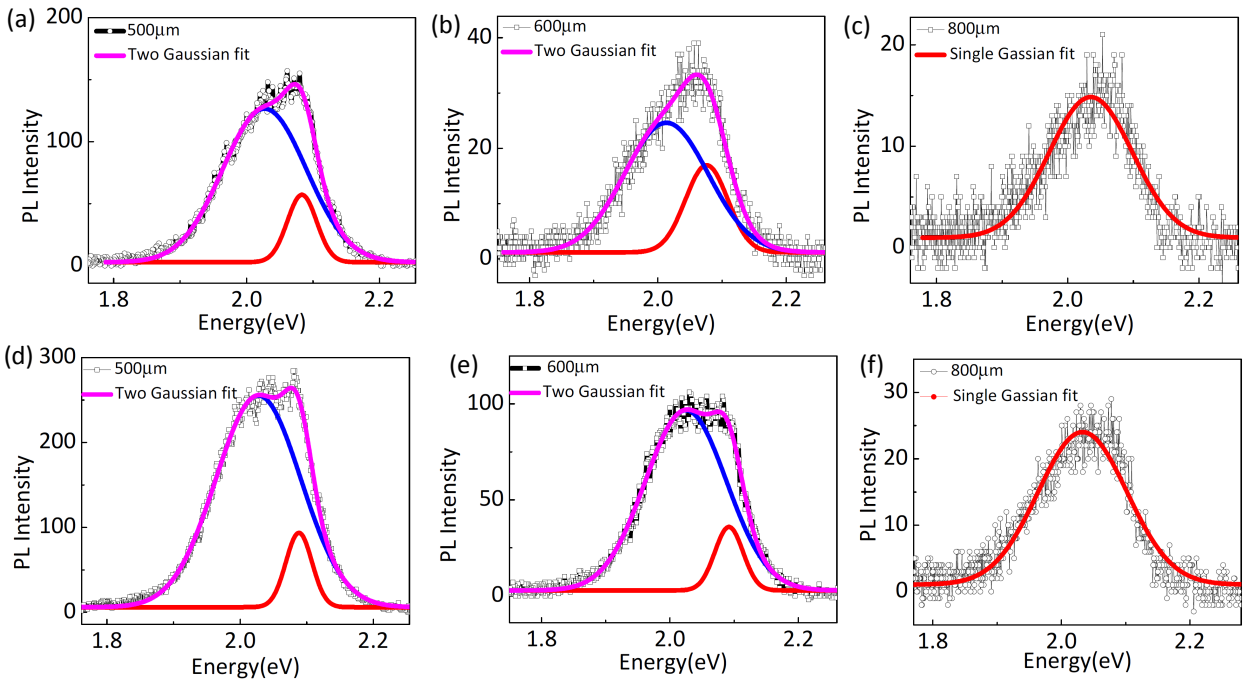

FIG. S9: PL spectra as a function of the distance between excitation and detection regions (X) for the C_3-configuration excited at $X = 0$ μm: (a), (b), (c), and excited at $X = 500$ μm (reverse mode): (d), (e), (f).

DISTANCE DEPENDENCE OF THE PL INTENSITY PROFILE

The distance dependence of the PL intensity for the SQD/plasmon lattice optical devices were measured by exciting the sample with a top objective 10X (NA = 0.20) using unpolarised 514 nm CW laser and collecting the PL from an objective, 50X (NA = 0.50) with larger collection efficiency. We use a higher NA=0.5 objective which has larger collection efficiency, in order to collect the distance dependence PL intensity data which suffers from poor statistics, especially at larger distance away from the excitation beam. However, the same objective when used to collect PL spectra within the excitation volume is not suitable for observing the strongly coupled modes which are highly dispersive and the larger collection efficiency leads to integration of this dispersive effect. This can be alleviated with smaller collection angle and lower NA = 0.2 objectives which show clear splitting, as shown in spectra in Fig. 4. Such objectives, on the other hand, are unsuitable for collecting propagation length data away from the excitation volume, effectively due to their inherently lower collection efficiency. To measure the PL from SQD regions displaced from the excitation region, the bottom objective was moved in the X-direction as shown in Fig. S7.

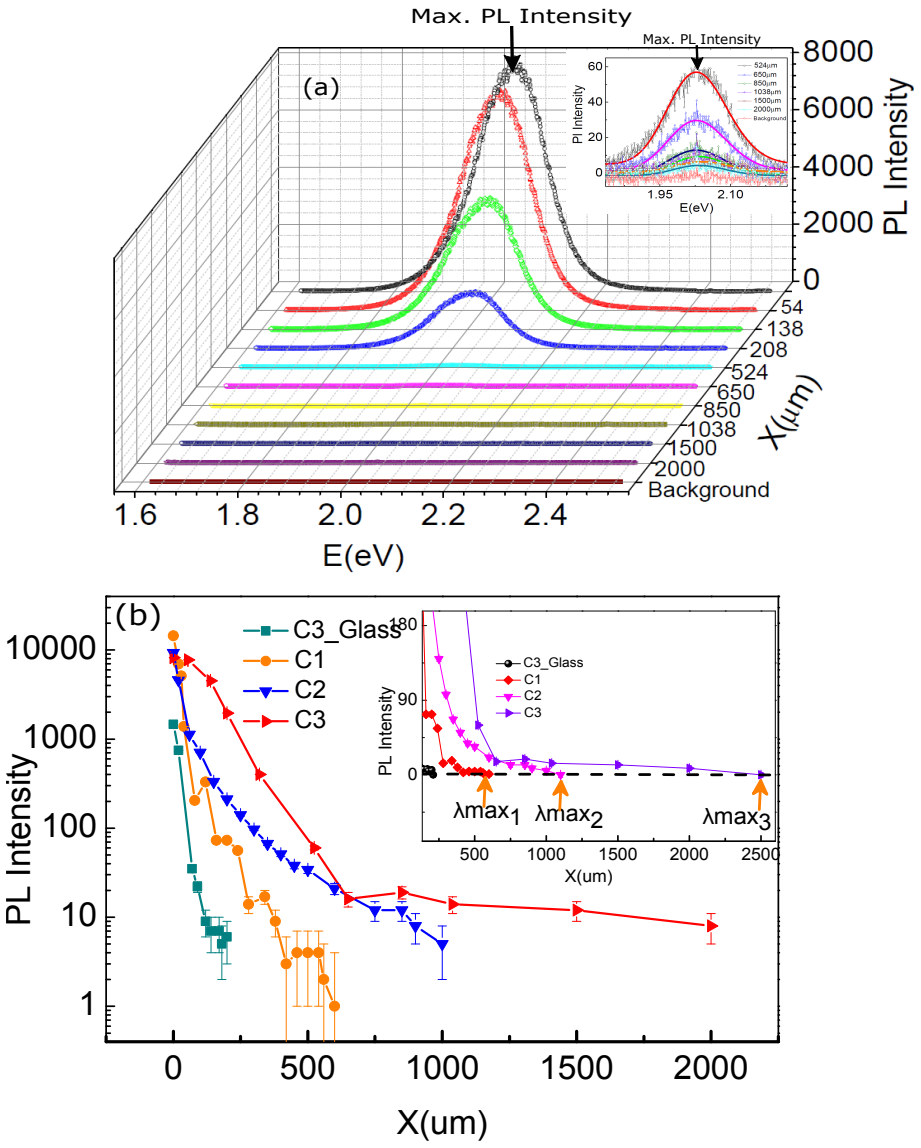

FIG. S10: Distance-dependent PL spectra at different X values using the larger collection efficiency objective, 50X,(NA=0.50). Inset: Distance-dependent PL spectra for larger X positions. (b) Distance-dependent PL intensity profile for configuration C_1, C_2, C_3 with densities $\rho_1 \approx 6.25\text{e}3/\mu\text{m}^3$, $\rho_2 \approx 3.13\text{e}4/\mu\text{m}^3$, $\rho_3 \approx 6.25\text{e}4/\mu\text{m}^3$. The inset shows a zoomed image of the lower PL intensity part of the distance profile. λ_{Max1}, λ_{Max2}, λ_{Max3} are the maximum propagation lengths of the PL spectra for configurations C_1, C_2, C_3 respectively (as indicated by arrows).

The measured distance-dependent intensity profile inside the excitation region is a convolution of the point spread function (PSF) of the excitation objective, 10X (NA=0.20) and collection objective, 50X (NA=0.50). A theoretical estimate of the full width at half maxima (FWHM) of the resultant point spread function is $\sim 40\ \mu$m [6]. The measured distance-dependent intensity pro-

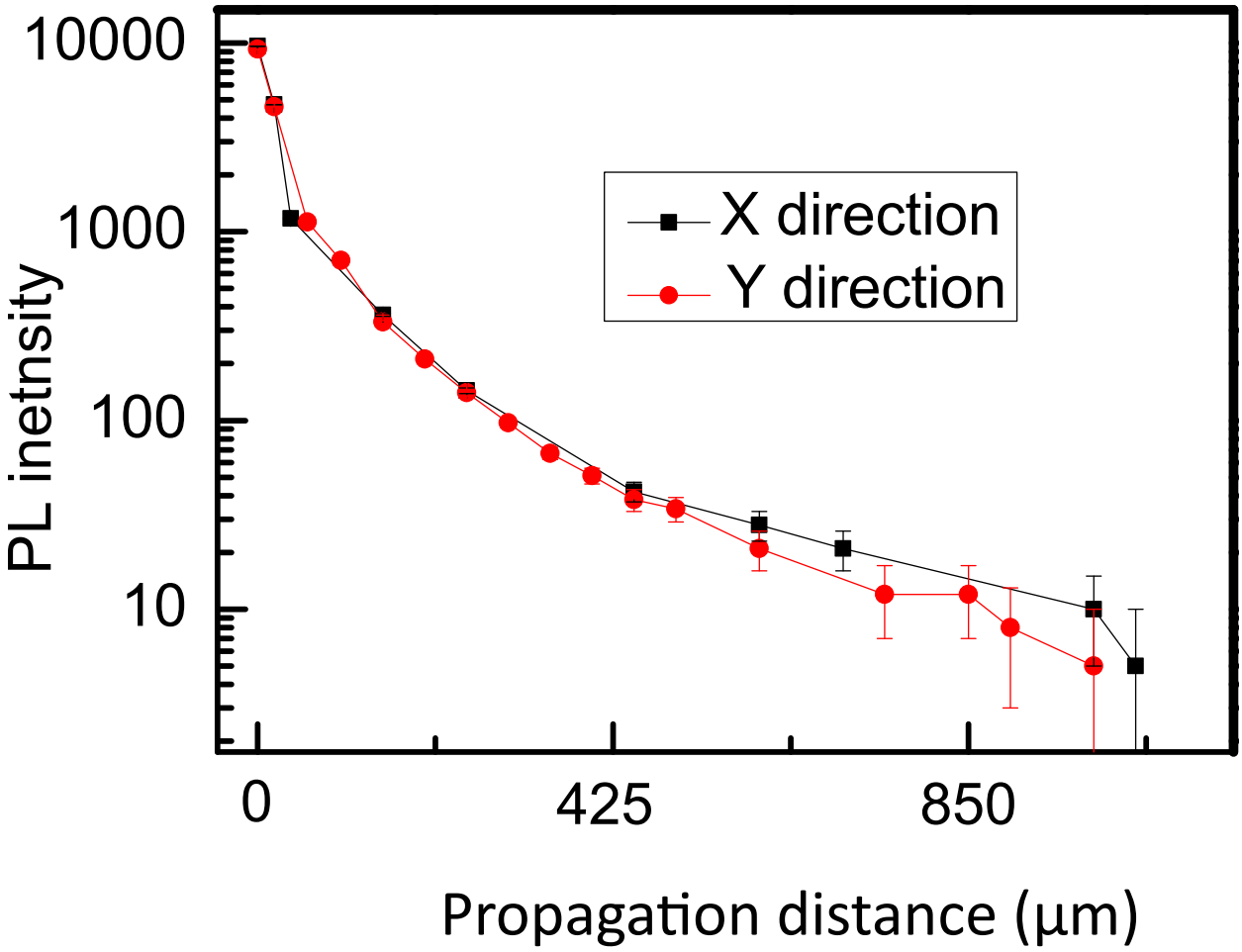

FIG. S11: Propagation distances measured in the X and Y directions for the C_2 configuration.

file of SQD/glass system shows a Gaussian profile with FWHM~ 35 μm which is consistent with theoretical estimates.

Figure S10(a) shows the PL spectra of SQD/plasmon lattice at different X positions. Figure S10(b) shows the distance dependence of the intensity profile (on a log-linear scale) where the maximum PL intensity for each X is plotted. The Fig. S9(b) inset shows a zoomed image on a linear scale to show the propagation lengths, λ_{max1}, λ_{max2}, λ_{max3} where PL spectra goes to background for C_1, C_2, C_3 respectively.

PROPAGATION DISTANCES ALONG THE X AND Y DIRECTIONS

We did measure propagation distances for the C_2 configuration, which corresponds to 5 SQD monolayers and indicated by the green curve in Fig. 5 (main text) for both the X and Y directions,

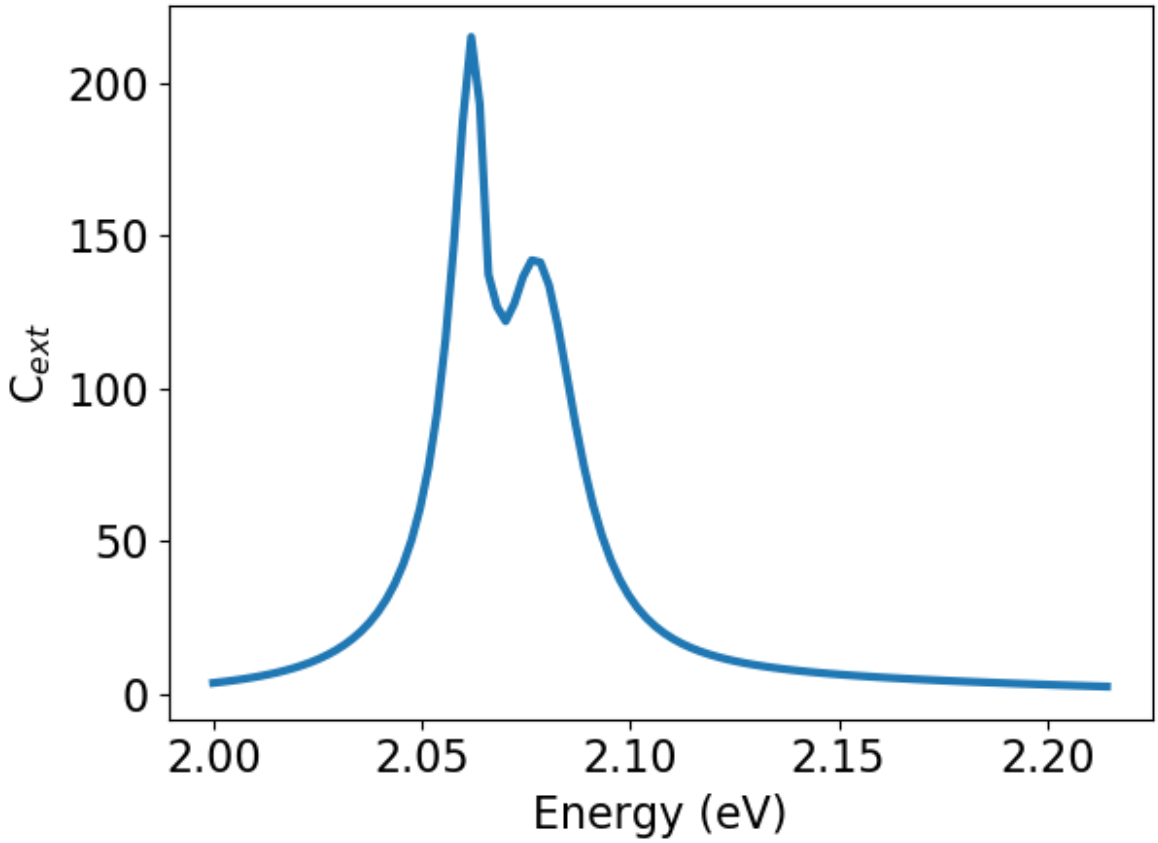

FIG. S12: Extinction coefficient from coupled dipole model.

as shown in Fig. S11. The propagation lengths appear to be very similar as expected from the symmetry of the system.

ADDITIONAL COUPLED DIPOLE RESULTS

The coupled dipole model can also be used to predict the extinction cross-section using,

$$C_{ext} = \frac{4\pi k_o}{|E_o|^2} \sum_k \mathrm{Im}[\mathbf{E}^*_{o,k} \cdot \mathbf{P}_k], \tag{4}$$

where E_o is the magnitude of the incident electric field. In Fig. S12, We plot the results for a 1D array of NPs coupled to SQDs as described in the main text. These results clearly demonstrate the energy splitting in agreement with the experiment, providing further validity for the coupled dipole model.

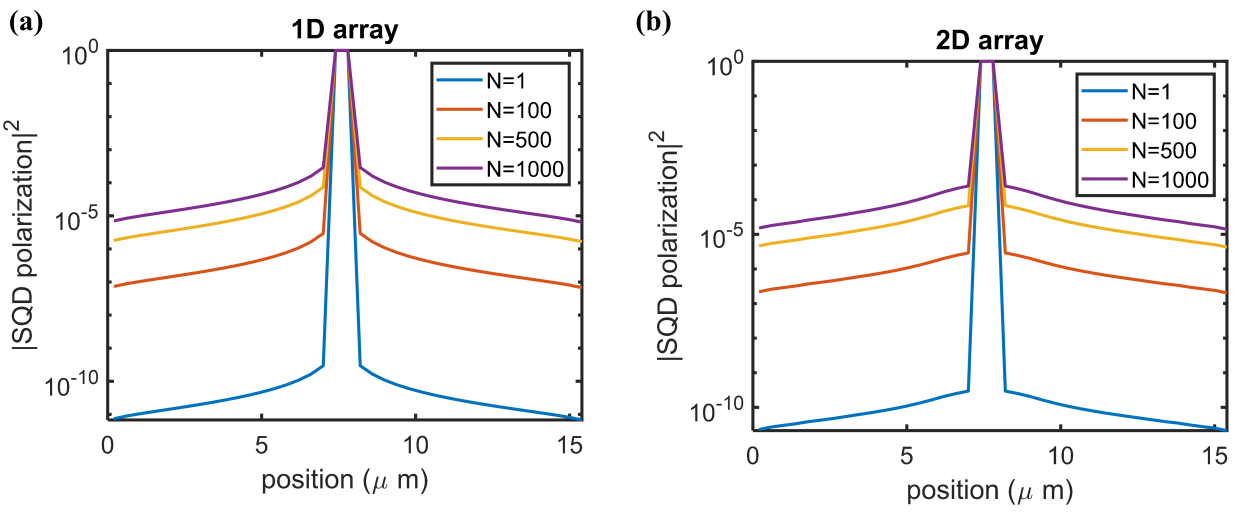

FIG. S13: Comparison between 1D and 2D array results of the coupled dipole model.

Comparison between 1D and 2D array results. In addition to the results provided in the main manuscript for a 1D coupled dipole array, we also provide evidence that concentration-dependent energy propagation also occurs for 2-dimensional nanoparticle arrays, shown in Fig. S13. The main difference between the 1D NP array and 2D NP array calculations involves the decoupling of the large $3N \times 3N$ linear system of equations, i.e. Eqs. (3) and (4) of the main manuscript. In the 1D case, the linear system of equations decouples cleanly into three separate $N \times N$ blocks, making it possible to simulate systems with a very large particle number. In the 2D case, the linear system of equations decouples into two blocks of size $2N \times 2N$ and $N \times N$ respectively. The $2N \times 2N$ sub-block mixes the $x-$ and $y-$ polarization components of the quantum dots and nanoparticles. Figure S13 confirms that concentration-dependent energy propagation persists in the 2D case. Additional polarization profile plots are shown in Fig. S14, corresponding to small SQD concentration ($N_{eff} = 1$) and Fig. S15 corresponding to a large QD concentration (N_{eff}=1000). The coupled dipole simulations were performed for a 40×40 nanoparticle 2D grid with quantum dots in between. A square illumination region in the center of the grid directly excites a 2×2 quantum dot array. All of these results are calculated under steady-state conditions with all figures normalized with respect to their maximum values.

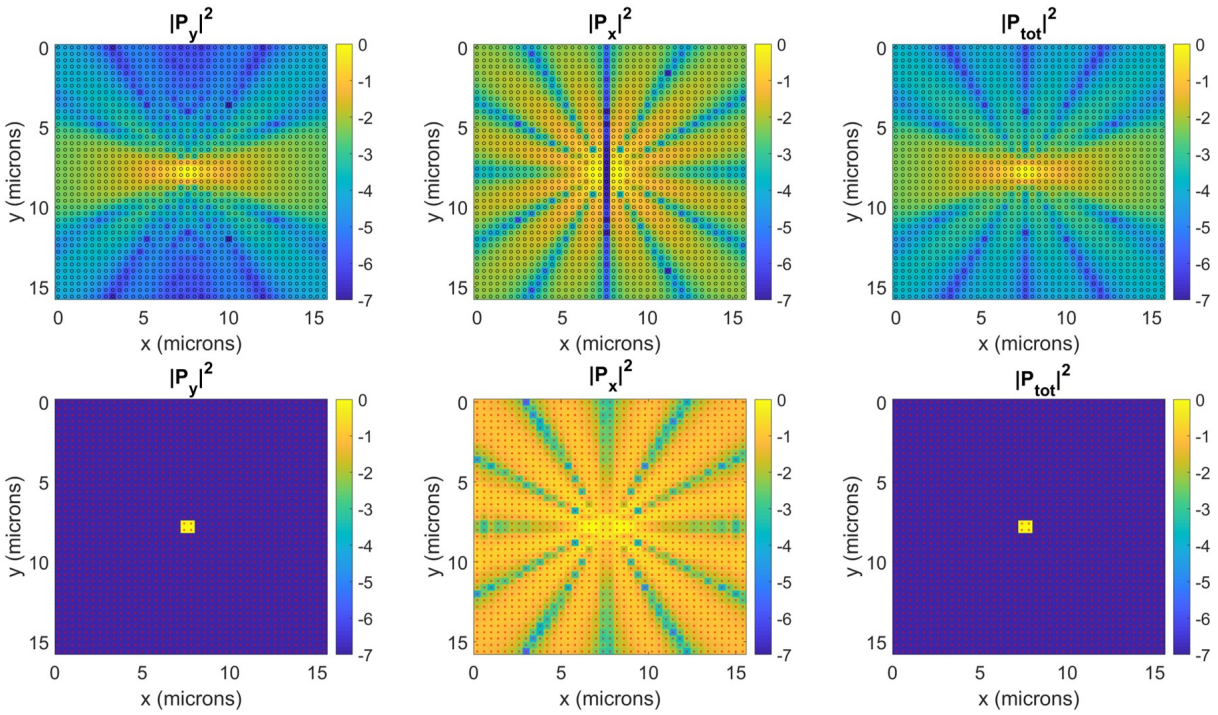

FIG. S14: 2D array polarization profile with concentration dependence N = 1. Top Row: polarization profile for nanoparticles. Bottom Row: polarization profile for quantum dots. All plots are normalized to their respective maxima with the color bar defined in logarithmic scale.

PHENOMENOLOGICAL CQED MODEL

To study the energy transfer between SQD regions, we model the experimental system using cavity quantum electrodynamic (cQED). We use the Hamiltonian

$$\hat{H} = \hat{H}_0 + \hat{H}_{SQD-SLR} + \hat{H}_d(t), \tag{5}$$

where $\hat{H}_0$ is the bare system Hamiltonian, $\hat{H}_{SQD-SLR}$ represents the coupling between the SQD regions and the SLR, and $\hat{H}_d$ is the laser driving field. To calculate the emission spectrum, we first start with the bare system Hamiltonian, containing the oscillator terms,

$$\hat{H} = \omega_{SQD}\hat{a}_1^\dagger\hat{a}_1 + \omega_{SLR}\hat{b}^\dagger\hat{b}, \tag{6}$$

where $\hat{a}_1$ is the annihilation operator representing the SQD region, $\hat{b}$ is the annihilation operator representing the SLR, and ω_{QD} (ω_{SLR}) is the SQD (SLR) oscillator frequency. The SQD region and SLR are coupled through

$$\hat{H}_{SQD-SLR} = g(X)(\hat{a}_1^\dagger\hat{b} + \hat{a}_1\hat{b}^\dagger), \tag{7}$$

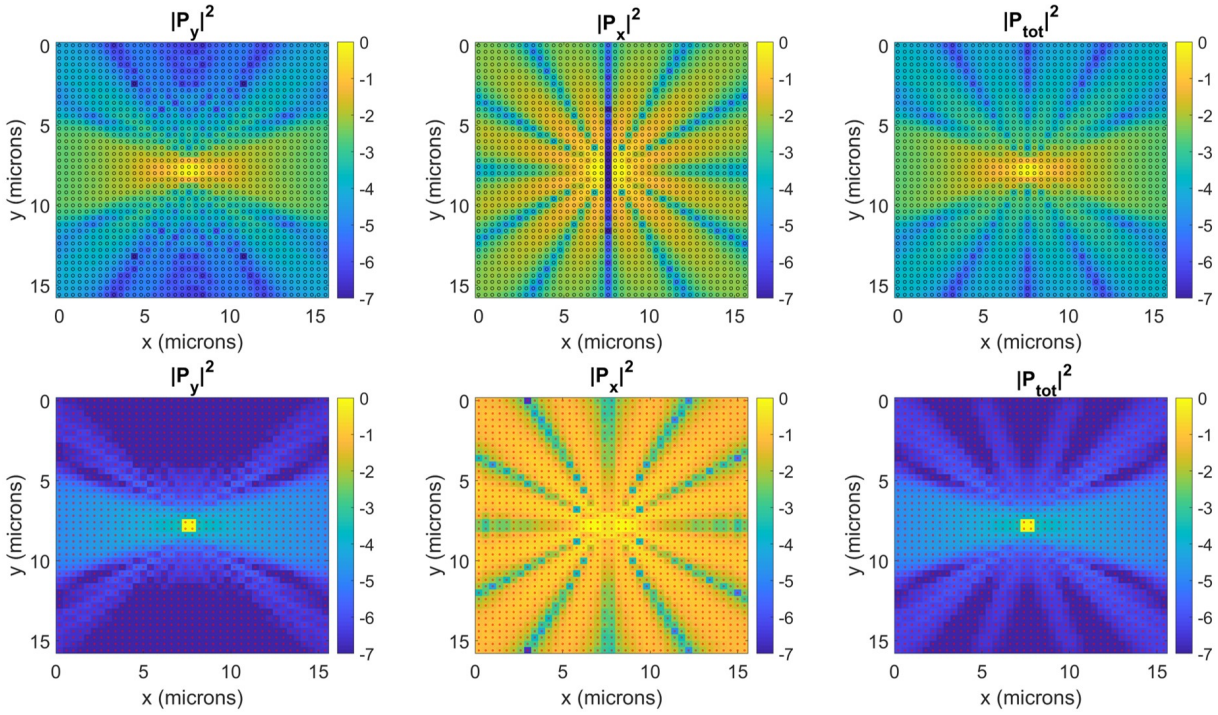

FIG. S15: 2D array polarization profile with concentration dependence N = 1000. Top Row: polarization profile for nanoparticles. Bottom Row: polarization profile for quantum dots. All plots are normalized to their respective maxima with the color bar defined in logarithmic scale.

where $g(X)$ is the fit to the experimentally measured splittings as a function of X, the distance from the excitation spot. We model the effect of the CW laser (resonant with the absorption peak of the SQD) as incoherent pumping of the SQD through a Lindblad superoperator

$$L_p(\hat{\rho}) = \frac{E_0}{2} D[a_1^\dagger](\hat{\rho}), \tag{8}$$

where E_0 is the strength of the CW pulse and $D[O]\hat{\rho} = 2O\hat{\rho}O^\dagger - O^\dagger O\hat{\rho} - \hat{\rho}O^\dagger O$. Within this model, the direct dot-dot coupling is ignored due to its low strength. We also include quantum dot and plasmon spontaneous emission via Lindblad superoperators,

$$L(\hat{\rho}) = \frac{\gamma_{S\,LR}}{2} D[b]\hat{\rho} + \frac{\gamma_{S\,QD,s}}{2} D[a_1]\hat{\rho} + \gamma_{S\,QD,d} D[a_1^\dagger a_1]\hat{\rho}, \tag{9}$$

where $\gamma_{S\,LR}$ ($\gamma_{S\,QD,s}$) is the SLR (QD) spontaneous emission rate and $\gamma_{S\,QD,d}$ is the SQD dephasing rate. For calculation of the emission spectrum, no laser pulse ($\hat{H}_d$ term) was used. We use the two-time correlation function to calculate the emission spectra. The parameters of our model are fit to the experimental data and are listed in Table II.

To calculate the energy propagation and transfer, we add additional SQD regions similarly to the original, incoherently pumped SQD region, except we do not include the incoherent pumping and the coupling strength g is treated as a function of distance. To study energy transfer, we had another SQD region which was coherently excited by a laser pulse,

$$\hat{H}_d(t) = E_p(t)\mu_{SQD}\cos(\omega_L t)(\hat{a}_2 + \hat{a}_2^\dagger) \tag{10}$$

where $E_p(t)$ is the time dependent pulse strength, ω_L is the laser frequency, and μ_{SQD} is the SQD region dipole strength.

TABLE II: Parameters of the cQED model.

Param	Description	Value
ω_{SQD}	SQD Frequency	2.066 eV
ω_{SLR}	Plasmon Frequency	2.0943 eV
ω_L	Laser Pulse Frequency	2.41 eV
$\gamma_{SQD,d}$	SQD Region Dephasing	50 meV
$\gamma_{SQD,s}$	SQD Region Spontaneous Emission	190 neV
γ_{SLR}	Plasmon Spontaneous Emission	31 meV
μ_{SQD}	SQD Region Dipole Moment	30 Debye
g	SQD-SLR Coupling	10-50 meV

Given the possible existence of relatively long range ($\approx 600\ \mu$m) ESLR mode, we now look at the coupling of spatially separated SQD regions to such a mode using a phenomenological cQED model. We simulate a phenomenological model of the system, consisting of the QD regions and one long-range SLR. Each SQD region is treated as a truncated, giant harmonic oscillator (in a Tavis-Cummings like fashion), representing the ensemble by only one quantum system. This is schematically shown in the inset of Fig. S16, which shows three such regions coupled to the single SLR. We model the laser as an incoherent pump of the giant harmonic oscillator, since our laser is pumping the 514 nm absorption transition, which then relaxes to the 590 nm state, resonant with the SLR. We include SQD spontaneous emission and dephasing, as well as SLR relaxation. The parameters of our model are fit to the experimental data. We first show that this cQED model gives qualitatively correct results for the emission spectra, as shown in the main text, Fig. 3(d). Due to the slight detuning of the SLR and SQDs, the actual SQD-SLR coupling is slightly smaller than

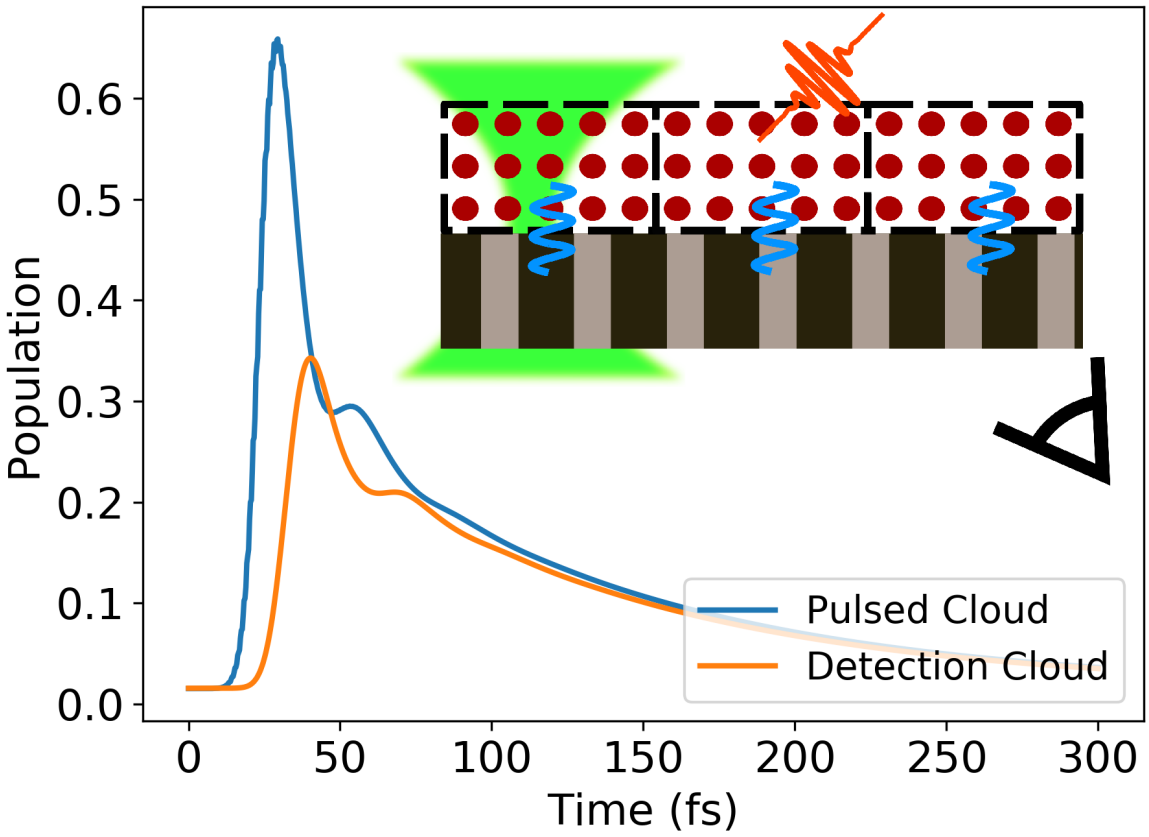

FIG. S16: Energy transfer through polariton mode. Inset: Schematic of proposed experiment.

half the splitting, leading to couplings strengths for the three densities of g = 9.5, 26, 41 meV, respectively.

With qualitative agreement between our phenomenological model and the experimental data, we now explore long-range coupling between distant SQD regions. Direct coupling between the two SQD regions is neglected. In this model, we simulate three quantum systems: the incoherently pumped SQD region within the laser spot, the long-range SQD-SLR, and a distant SQD region. In this model, we have effectively traced away all of the SQDs that are not within the excitation or detection regions. These SQDs are implicitly included due to the assumed long-range nature of the polariton mode, predicted by the coupled dipole model. We use a distance dependent coupling fit to measurements of the splitting at different detection spots. Outside the first 150 μm there is a decline in the measured splitting; as such, the effective coupling also declines. However, since the splitting can be measured up until 600 μm, the detection region is still coupled to the long-range

ESLR mode.

Though we see relatively long energy propagation in our experiments of $\approx 600\ \mu$m, we do not directly see coherent energy transfer between SQD regions, due to the CW laser and resulting incoherent pumping of the SQDs. To directly observe this, we propose an experiment consisting of our current setup with the addition of a laser pulse. This laser will coherently excite one SQD region away from the CW excitation. The excitation of the SQD region can then be transferred, through the long-range ESLR mode, to a separate SQD region, where a time-dependent detection of the emission is taken. The results of a simulation of such an experiment are shown in Fig. S16. The initial rise in the population of the excited SQD region leads to a rise in the population of the detection region.

[1] K. Lambert, R. K. Capek, M. I. Bodnarchuk, M. V. Kovalenko, D. Van Thourhout, W. Heiss, and Z. Hens, Langmuir **26**, 7732 (2010).

[2] C. Indukuri, R. K. Yadav, and J. Basu, Nanoscale **9**, 11418 (2017).

[3] A. Gole, N. R. Jana, S. T. Selvan, and J. Y. Ying, Langmuir **24**, 8181 (2008).

[4] I. Lokteva, N. Radychev, F. Witt, H. Borchert, J. Parisi, and J. Kolny-Olesiak, The Journal of Physical Chemistry C **114**, 12784–12791 (2010).

[5] H. Groß, J. M. Hamm, T. Tufarelli, O. Hess, and B. Hecht, Science advances **4**, eaar4906 (2018).

[6] L. Novotny and B. Hecht, *Principles of nano-optics* (Cambridge University Press, 2012).